Combined effects of radiation damage and He accumulation on bubble nucleation in $Gd_2Ti_2O_7$

Caitlin A. Taylor [a, *], Maulik K. Patel [a], Jeffery A. Aguiar [b, c], Yanwen Zhang [d, a], Miguel L. Crespillo [a], Juan Wen [e, f], Haizhou Xue [a], Yongqiang Wang [f], William J. Weber [a, d]

[a] Department of Materials Science and Engineering, The University of Tennessee, Knoxville, TN 37996, USA
[b] Fuel Performance and Design Department, Idaho National Laboratory, Idaho Falls, ID 83415-6188, USA
[c] Material Science Center, National Renewable Energy Laboratory, Golden, CO 80220, USA
[d] Materials Science and Technology Division, Oak Ridge National Laboratory, Oak Ridge, TN 37831, USA
[e] School of Nuclear Science and Technology, Lanzhou University, Lanzhou, Gansu 730000, China
[f] Materials Science and Technology Division, Los Alamos National Laboratory, Los Alamos, NM 87545, USA

HIGHLIGHTS

- He bubbles not formed in amorphous $Gd_2Ti_2O_7$ implanted with 2×10^{16} He/cm^2, even after additional irradiation at 300 to 700 K.
- He bubbles, 1.5 and 2.1 nm diameter, respectively, observed in amorphous and pristine $Gd_2Ti_2O_7$ implanted to 2×10^{17} He/cm^2.
- The critical He dose for bubble nucleation is estimated to be 6 at.% He.

GRAPHICAL ABSTRACT
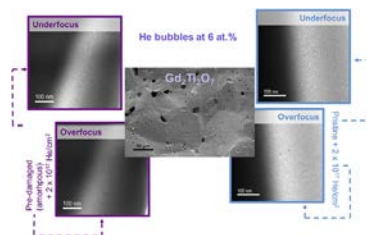
ABSTRACT

Pyrochlores have long been considered as host phases for long-term immobilization of radioactive waste nuclides that would undergo α-decay for hundreds of thousands of years. This work utilizes ion-beam irradiations to examine the combined effects of radiation damage and He accumulation on bubble formation in $Gd_2Ti_2O_7$ over relevant waste-form timescales. Helium bubbles are not observed in pre-damaged $Gd_2Ti_2O_7$ implanted with 2×10^{16} He/cm^2, even after post-implantation irradiations with 7 MeV Au^{3+} at 300, 500, and 700 K. However, He bubbles with average diameters of 1.5 nm and 2.1 nm are observed in pre-damaged (amorphous) $Gd_2Ti_2O_7$ and pristine $Gd_2Ti_2O_7$, respectively, after implantation of 2×10^{17} He/cm^2. The critical He concentration for bubble nucleation in $Gd_2Ti_2O_7$ is estimated to be 6 at.% He.

© 2016 Elsevier B.V. All rights reserved.

1. Introduction

Nuclear waste from reactors and legacy weapons programs contains actinides, such as ^{239}Pu, ^{237}Np, ^{241}Am, and ^{244}Cm. Long-lived actinides (e.g. ^{239}Pu with a half-life of 24,100 years and ^{237}Np with a half-life of 2.1 million years) pose the greatest health threat [1]. In addition, substantial quantities of excess Pu from retired weapons [2] and Pu separated from commercially-generated spent fuel currently exist in several countries [3]. One potential solution involves immobilization of the actinides in nuclear waste-forms, which are then deposited in a geological repository for long-term storage. Current host matrices under

* Corresponding author.
  E-mail address: ctayl105@vols.utk.edu (C.A. Taylor).

consideration for use as nuclear waste-forms include glasses and crystalline ceramics. Glasses provide the simplest approach to actinide immobilization, as fewer separation steps are required; however, actinide solubility in glasses is a concern for separated actinides [2]. Multiphase crystalline waste-forms can be tailored for complex nuclear wastes, with one or more phases acting as host phases for actinides. In the case of separated actinides, both single-phase and multiphase waste-forms have been proposed [2,3]. Crystalline ceramics, while more difficult to fabricate, provide improved chemical durability over glass waste-forms due to actinides being incorporated and bonded into lattice site positions. In addition, crystalline ceramics offer a more predictable landscape for actinide immobilization than less durable materials that rely heavily on engineered barriers and the geological repository mineralogy itself to contain the radioisotopes. Natural analogues to crystalline ceramics provide validation data on the performance of mineral-like ceramics under long-term storage conditions. Complex ceramics, e.g. pyrochlore, zirconolite, and monazite, are particularly useful as they offer a variety of lattice sites, allowing for incorporation of actinides of varying size and valence state [1,4].

Actinide-containing waste-forms must be able to withstand α-decay from the incorporated actinides for hundreds of thousands of years, with the rate of α-decay varying with actinide type and concentration. Each α-decay event will produce one α-recoil nucleus (~100 keV) and one α-particle, or He nucleus, (~5 MeV), resulting in significant damage and He accumulation over geological time. This work focuses on pyrochlores, an $A_2B_2O_7$ structure, where actinides can occupy the A-site (2+, 3+) and B-site (4+, 5+). The pyrochlore matrix has long been considered as a potential actinide immobilization host phase [5–8]. Ion-irradiation studies have shown that $Gd_2Ti_2O_7$, like all other titanate pyrochlores, amorphizes under irradiation [9–11]. Previous work on $Gd_2Ti_2O_7$ doped with ^{244}Cm showed that amorphization results from the overlap of amorphous tracks produced by α-recoils and spontaneous fission fragments [12]. $Gd_2Ti_2O_7$ becomes fully amorphous at a dose of ~0.2 dpa or within the first several hundred years of waste-form storage depending on actinide content [9]. The leach rates of Gd and Ti ions from irradiated $Gd_2Ti_2O_7$ placed in 90 °C nitric acid solution increased by a factor of 15 due to irradiation-induced amorphization [13]. While the amorphous state is stable, helium accumulation may result in bubble nucleation and growth over geological time, which could place additional stresses on the material that instigate crack formation. Cracks would provide a direct path for groundwater to enter the waste-form, potentially increasing the leach rate of radioactive material. Helium bubbles several nanometers in diameter have been observed in fluorite-structured materials (e.g. AmO_2 [14] and yttria-stabilized zirconia [15]) and in amorphous borosilicate glass [16,17]; however, to the best of our knowledge, He bubbles have not been previously studied in any pyrochlore composition. Transmission electron microscopy (TEM) measurements revealed bubble formation and growth after implantation of a few atomic percent He in nuclear glass [16,17], and similar behavior might be expected in amorphous $Gd_2Ti_2O_7$. In this work, various ion-beam irradiations and He implantation experiments were performed to study the effects of combined radiation damage and He accumulation on bubble nucleation and growth in the pyrochlore $Gd_2Ti_2O_7$ over relevant waste-form timescales.

2. Experimental methods

$Gd_2Ti_2O_7$ samples were prepared using conventional solid-state synthesis by mixing Gd_2O_3 and TiO_2 powders in stoichiometric ratios, ball milling, pressing the powders into individual pellets using a room temperature uniaxial press, and sintering in air.

Samples were ~12.7 mm in diameter after sintering and estimated to be 94% theoretical density using the Archimedes method. The as-synthesized samples, which had a typical grain size of 50–80 μm (Fig. 1), were polished using diamond lapping film down to 1 μm and finished using a 0.02 μm colloidal silica solution to remove residual polishing damage. Table 1 summarizes all irradiation conditions utilized in this work. All samples were pre-damaged with 7 MeV Au^{3+} to a fluence of 2.2×10^{15} Au/cm^2 (6 dpa at the damage peak) using a 3 MV tandem accelerator at the University of Tennessee's Ion Beam Materials Laboratory [18]. The ion flux was kept constant (8.1×10^{11} $ions/cm^2/s$) during the Au irradiation, and the ion beam was rastered (at scanning frequencies of 517 and 64 Hz for the horizontal and vertical directions, respectively, and a current density of 3.89 nA/mm^2) over an irradiated area of 10.2×10.2 mm to ensure a uniform irradiation over a majority of the pellet surface. A glass scintillator and a CCD camera were used to accurately locate the ion beam. Following He implantations (described below), some samples were further irradiated at 300, 500 and 700 K under the same 7 MeV Au^{3+} conditions. In the case of high temperature irradiation of the He-implanted samples, the temperature was controlled using a HRN (LPS-800-1) heater controller from Thermionics Northwest Inc. The room temperature Au irradiations produced a beam heating of ~50 °C, as measured by a type K thermocouple at the sample surface. More details about the high temperature irradiations capability can be found in the description of the UT-IBML facility [18]. The Au irradiation dose in these samples exceeds that required for full amorphization (Fig. 2) and corresponds to the total damage accumulation expected over 50–1000 years in a waste form containing 5 wt% minor actinides and 1000–10,000 years in a waste-form containing 20 wt% ^{239}Pu [1,4], as shown in Fig. 2. This pre-damage step induces the pyrochlore to amorphous phase transformation that would occur due to α-recoil damage during interim or early storage times (several hundred to several thousand years); furthermore, this phase transformation will occur prior to any significant He accumulation in an actual nuclear waste-form. Samples were implanted with either 200 keV He^+ to fluences of 2×10^{15} and 2×10^{16} He/cm^2 (0.1 and 1.0 at.% He at the peak, projected range (R_p ~ 900 nm) or with 65 keV He^+ to a fluence of 2×10^{17} He/cm^2 (12 at.% He at the peak, R_p ~ 450 nm) using the 200 kV Danfysik Research Implanter at Los Alamos National Laboratory's Ion Beam Materials Laboratory. The ion fluxes utilized for the He implantations were 1.1×10^{13} $ions/cm^2/s$ for the 200 keV implantations and 7.39×10^{12} $ions/cm^2/s$ for the 65 keV implantations. Damage dose and He concentration values were simulated using full cascade mode in the Monte Carlo code Stopping and Range of Ions in Matter (SRIM) [19], with all
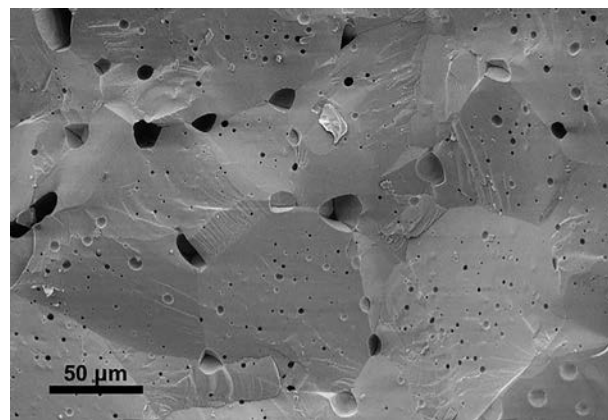

Fig. 1. SEM backscattered electron image obtained from a fractured as-synthesized $Gd_2Ti_2O_7$ pellet.

Table 1
Summary of irradiation conditions utilized to simulate α-recoil damage and He accumulation in $Gd_2Ti_2O_7$. "Pre-damage" refers to damage produced prior to He implantation and "post-damage" refers to damage produced after the He implantation. In the "He implantation" column, the number in parentheses indicates the peak He concentration. Irradiations identical to Samples 2–5, but implanted with 200 keV He+ to 2×10^{15} He/cm² (0.1 at.% He at the peak) instead of 2×10^{16} He/cm², were also performed. All pre-damage and He irradiations were performed at room temperature. Sample 7 was a FIB lift-out taken from the very edge of the sample, which was a region undamaged by during the Au irradiation. The right column states whether or not He bubbles were observed in TEM, and, if so, the mean bubble diameter.

Sample#	Pre-damage	He implantation (peak He conc., at.%)	Post-damage	He bubbles?
1	7 MeV Au³⁺ 2.2×10^{15} ions/cm²	x	x	No
2	7 MeV Au³⁺ 2.2×10^{15} ions/cm²	200 keV He+ 2×10^{16} ions/cm² (1.0)	x	No
3	7 MeV Au³⁺ 2.2×10^{15} ions/cm²	200 keV He+ 2×10^{16} ions/cm² (1.0)	7 MeV Au³⁺ (RT) 2.2×10^{15} ions/cm²	No
4	7 MeV Au³⁺ 2.2×10^{15} ions/cm²	200 keV He+ 2×10^{16} ions/cm² (1.0)	7 MeV Au³⁺ (500 K) 2.2×10^{15} ions/cm²	No
5	7 MeV Au³⁺ 2.2×10^{15} ions/cm²	200 keV He+ 2×10^{16} ions/cm² (1.0)	7 MeV Au³⁺ (700 K) 2.2×10^{15} ions/cm²	No
6	7 MeV Au³⁺ 2.2×10^{15} ions/cm²	65 keV He+ 2×10^{17} ions/cm² (12.0)	x	Yes, 1.5 nm diameter
7	x	65 keV He+ 2×10^{17} ions/cm² (12.0)	x	Yes, 2.1 nm diameter

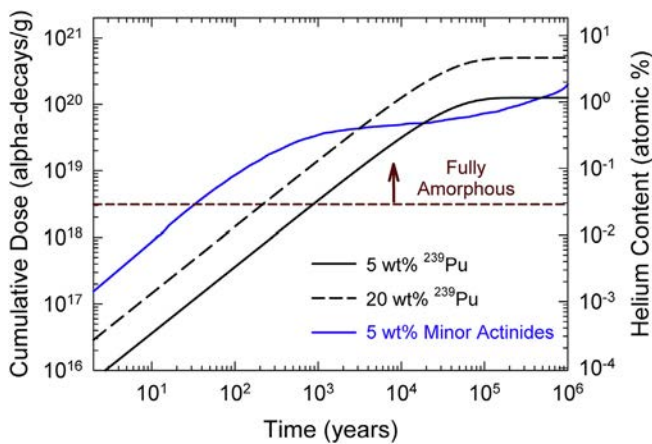**Fig. 2.** Expected dose and He content in $Gd_2Ti_2O_7$ over geological time for different actinide concentrations [1,4]. $Gd_2Ti_2O_7$ will be fully amorphous above the dose corresponding to the dashed line (3.1×10^{18} α-decays/g).

Fig. 3. TEM image obtained from $Gd_2Ti_2O_7$ after irradiation with 7 MeV Au³⁺ to a fluence of 2.2×10^{15} Au/cm². The corresponding dose (dpa) is shown with a dotted line. Electron diffraction was utilized to identify the irradiated depth, which is in reasonable agreement with the SRIM predicted implantation depth. SAED aperture size and locations are shown as circles below each diffraction pattern.

displacement energies set to 50 eV [1] and an assumed density of 6.575 g/cm³ (theoretical density), and using 2008 stopping powers. The Au and He irradiation energies were specifically chosen such that the 7 MeV Au³⁺ irradiation produced a thick amorphous layer that extended significantly deeper than the peak in He concentration. Moreover, the Au concentration peak (~1 μm from surface, ~0.06 at.%) is significantly deeper than the He concentration peak (~700 nm from surface for 200 keV He+), so as to preserve the chemical integrity near the He concentration peak where bubbles were expected to form. Calculated damage and concentration profiles are provided in Figs. 1–2 of the supplemental file for reference. It is worth noting that electronic stopping powers may be overestimated for heavy ions in a target containing light elements [20,21], such as the case for Au ions in $Gd_2Ti_2O_7$ in this work. To ensure pre-amorphization before He implantation, the thickness of the amorphous layer was confirmed using TEM (Fig. 3). Grazing-incidence x-ray diffraction (GIXRD) was also utilized to confirm amorphization, and is included in Fig. 3 of the supplemental file for reference. Helium implanted samples were characterized using
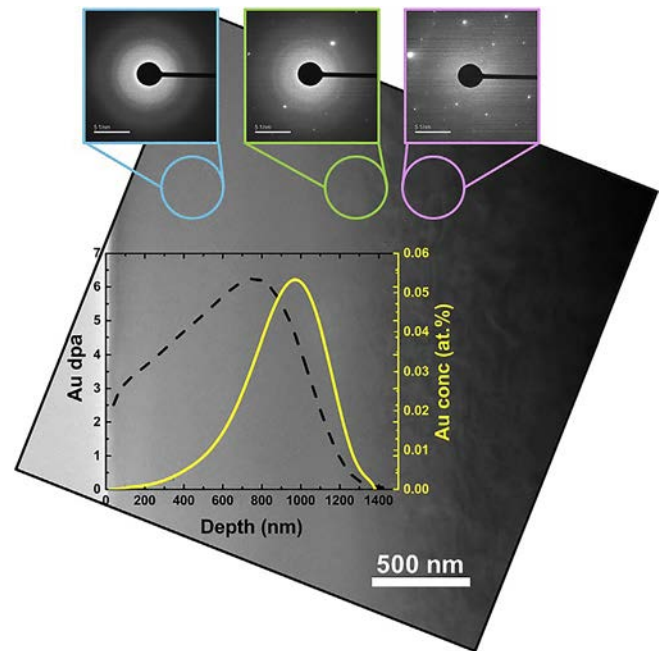
TEM to quantify the presence or absence of bubbles with the through-focus technique. Each sample was observed in the TEM while focused, and at all defocus values between −1 μm and +1 μm. Several magnifications were utilized to search for bubbles. The TEM image was focused by expanding the Fourier transform to the largest possible diameter. Defocus values may vary by an estimated ±100 nm due to error in finding the zero (focused) point. In underfocus conditions, bubbles or voids appear bright with a dark ring; while in overfocus conditions, they appear dark with a bright ring, due to Fresnel contrast. In all TEM observations, the smallest

possible objective aperture was utilized (ranging from 20 to 60 μm). The pre-damaged (Au irradiated) sample and all samples implanted with 2×10^{16} He/cm² were prepared by hand polishing cross-sections down to 5–10 μm thickness, and then final polished to electron transparency (<100 nm thickness) using a Gatan Precision Ion Polishing System (PIPS) with 4 keV Ar⁺. TEM imaging on the pre-damaged sample and all samples implanted with 2×10^{16} He/cm² was performed using a ZEISS Libra 200 MC, which is part of the Joint Institute for Advanced Materials (JIAM) Microscopy Center at the University of Tennessee, Knoxville. An FEI Nova 200 Nanolab Dual Beam focused ion beam (FIB) was utilized for preparing cross-sections of the samples implanted with 2×10^{17} He/cm². TEM imaging on the sample implanted with 2×10^{17} He/cm² was performed at the National Renewable Energy Laboratory (NREL) using an FEI Tecnai. Helium bubbles were quantified using the 'Analyze Particle' feature in ImageJ software [22], which determines the approximate cross-sectional area of each bubble. Outlines of the features selected by ImageJ are provided in the supplemental file (Figs. 8–9). Since the low contrast between bubbles and the amorphous $Gd_2Ti_2O_7$ makes image analysis difficult, the image analysis is subjective and results should only be utilized as a qualitative guide for understanding bubble density and size. The cross-sectional area of each bubble was converted to bubble diameter using a circular cross-sectional area approximation. Most bubbles observed in these samples were close to circular. The bubble size distribution was fit with a log-normal distribution to determine the average diameter. The error in bubble diameter was estimated as 2 Å based on the TEM image pixel size, which was 0.2 nm in both the pre-damaged + 2×10^{17} He/cm² images and the pristine +2 × 10¹⁷ He/cm² images.

3. Results

As referenced above, Table 1 summarizes the irradiation conditions and TEM observation results. Helium bubbles were not observed in pre-damaged $Gd_2Ti_2O_7$ implanted with 2×10^{16} He/cm² (peak concentration of 1.0 at.%), even after additional post-implantation irradiation with 7 MeV Au³⁺ to 2.2×10^{15} Au/cm² at 300, 500 and 700 K, as shown in the defocused images in Fig. 4. The irradiations at 500 and 700 K were intended to enhance the kinetics of bubble formation and mimic the kinetics occurring over a hundred thousand years. Based on these results, it is assumed that no bubbles are present at the lowest implantation fluence (2×10^{15}

He/cm²), and these samples were not further characterized by TEM.

Fig. 5 (a) provides an overview of the entire irradiated region in the sample pre-damaged and implanted with 2×10^{17} He/cm², in which the amorphous layer thickness corresponds to the SRIM predicted Au damage profile. Fig. 5 (b) and (c) provide TEM images from the SRIM-predicted He concentration peak region in both underfocused and overfocused conditions. The images indicate the presence of He bubbles near the resolution limit of the TEM (~1 nm in diameter) near the He concentration peak; the bubbles appear as small contrasting spots in Fig. 5 (b) and (c). Due to the amorphous background and instrument resolution limitations, bubbles were difficult to discern. At magnifications higher than those utilized in Fig. 5 (b) and (c), the visibility of bubbles in this material is even lower due to increased resolution of the noisy amorphous
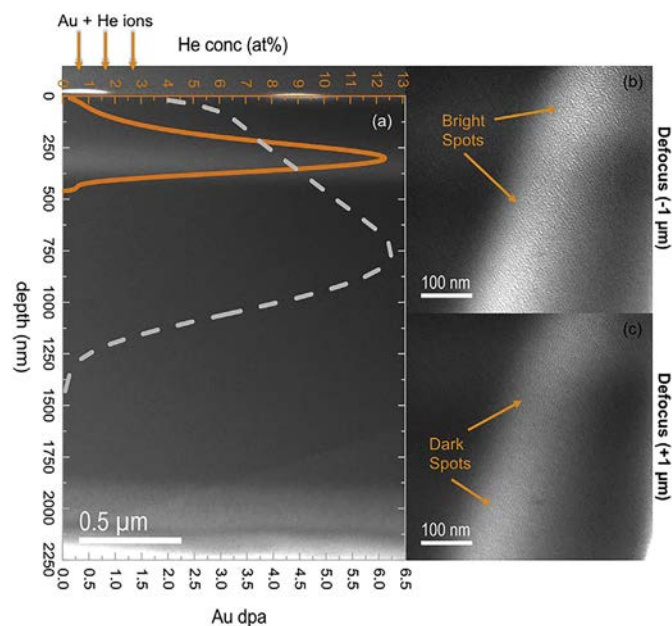

Fig. 5. TEM images obtained from $Gd_2Ti_2O_7$ irradiated with 7 MeV Au³⁺ to a fluence of 2.2×10^{15} Au/cm² and 65 keV He⁺ to a fluence of 2×10^{17} He/cm². An overview of the irradiated region is shown in (a), where the dashed line corresponds to the Au irradiation dose (dpa). Through-focus imaging at the helium implant peak clearly shows bubbles as bright spots in (b) underfocus and as dark spots in (c) overfocus.
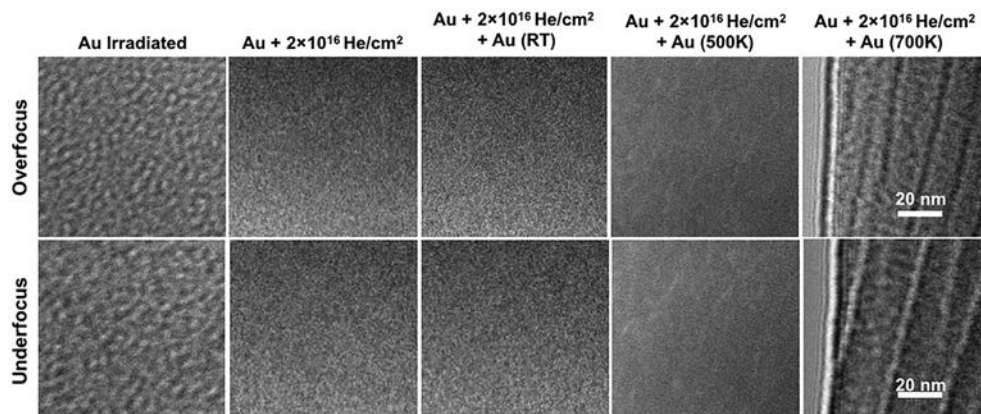

Fig. 4. TEM images shown at 250,000x (scale bar is equivalent for all images) with defocus values of ±1 μm obtained from all $Gd_2Ti_2O_7$ samples implanted with 200 keV He⁺ to a fluence of 2×10^{16} He/cm², and pre- or post-damaged with 7 MeV Au³⁺ to a fluence of 2.2×10^{15} Au/cm². Each sample was observed at defocus values between ±1 μm. Bubbles were not observed in any of the samples irradiated to this He fluence, even after post-irradiation damage at 700 K. In the images to the right (Au + 2 × 10¹⁶ He/cm² + Au 700 K), part of the surface was removed during the ion milling; the peak location was determined with reference to the amorphous/crystalline interface. Surface artifacts created during the sample preparation are highly visible in some of the images due to the high defocus values (±1 μm).

structure. Larger images are provided in Figs. 6–7 of the supplemental file.

A FIB lift-out was also taken from the very edge of the sample pre-damaged and implanted with 2×10^{17} He/cm^2. When observed in the TEM (Fig. 6 (a)), the sample was found to be amorphous only up to the depth of the *He damage range*, and not the Au damage range, as found elsewhere in the sample. This indicates that the very edge of the sample was not irradiated with Au, which is not unexpected under the irradiation conditions, but only implanted with He. SRIM simulations predict a He damage dose >0.2 dpa, i.e., the dose required to amorphize Gd$_2$Ti$_2$O$_7$ [9], from the surface to a
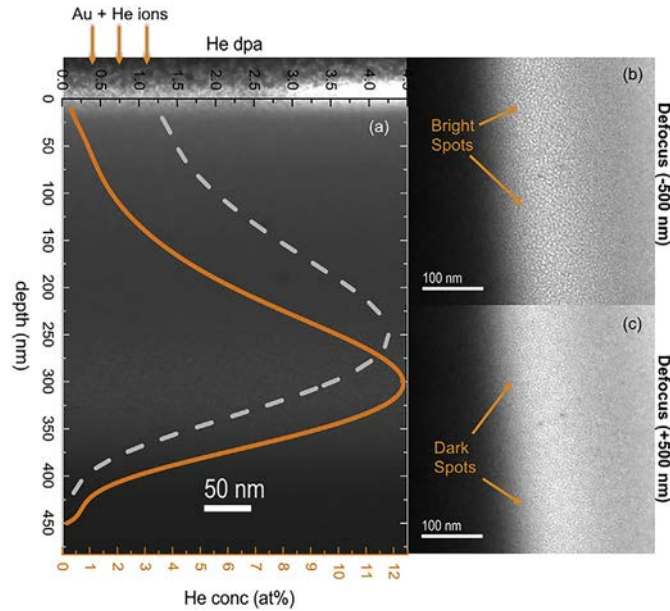

Fig. 6. TEM images obtained from pristine Gd$_2$Ti$_2$O$_7$ implanted with 65 keV He$^+$ to a fluence of 2×10^{17} He/cm^2. An overview of the irradiated region is shown in (a), where the dashed line corresponds to the He dose (dpa). Through-focus imaging at the helium implant peak clearly shows bubbles as bright spots in (b) underfocus and as dark spots in (c) overfocus.
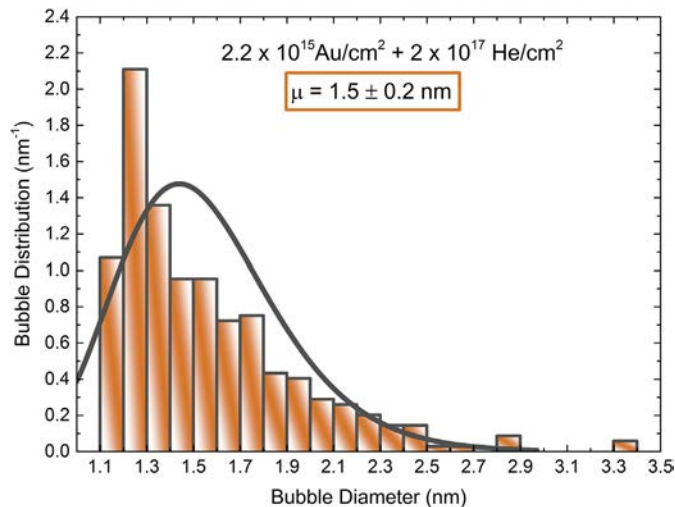

Fig. 7. Bubble size distribution measured from TEM images of Gd$_2$Ti$_2$O$_7$ irradiated with 7 MeV Au^{3+} to a fluence of 2.2×10^{15} Au/cm^2 and 65 keV He$^+$ to a fluence of 2×10^{17} He/cm^2. Line shows a normal distribution with a mean diameter of 1.5 ± 0.2 nm. Error is based on the pixel size in the TEM images. An example of the bubble outlines, as determined by ImageJ software during the image analysis, is provided in Fig. 9 of the supplemental file.
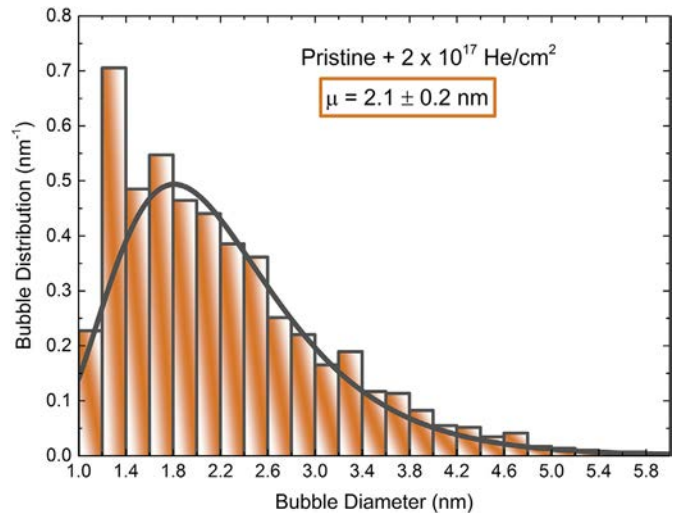

Fig. 8. Bubble size distribution measured from TEM images of Gd$_2$Ti$_2$O$_7$ implanted with 65 keV He$^+$ to a fluence of 2×10^{17} He/cm^2. Line shows a normal distribution with a mean diameter of 2.1 ± 0.2 nm. Error is based on the pixel size in the TEM images. An example of the bubble outlines, as determined by ImageJ software during the image analysis, is provided in Fig. 8 of the supplemental file.

depth of ~400 nm, which agrees with the amorphous layer thickness observed in the TEM image in Fig. 6 (a). If the edge of the sample had been implanted with Au, the amorphous layer would correspond to the SRIM predicted Au damage profile thickness (~1.3 μm), as was the case for the pre-damaged samples discussed above and shown in Fig. 3. It is therefore assumed that the very edge of the sample was not pre-damaged with Au, only implanted with He. In this TEM sample, which the authors consider as initially pristine pyrochlore Gd$_2$Ti$_2$O$_7$ implanted with 2×10^{17} He/cm^2, the bubbles are more clearly visible in the underfocused and overfocused imaging conditions, as shown in Fig. 6 (b) and (c). Bubbles are larger and of higher density than the pre-damaged (amorphous) Gd$_2$Ti$_2$O$_7$ sample implanted with the same He fluence. Larger images are provided in Figs. 4–5 of the supplemental file.

Bubble size distributions for the pre-damaged and pristine samples implanted to 2×10^{17} He/cm^2 are provided in Figs. 7 and 8. The mean bubble diameter is 1.5 nm in the pre-damaged implanted sample and 2.1 nm for the pristine implanted sample. In both samples, bubbles are first observed at a depth of ~200 nm, which corresponds to a He concentration of ~6 at.%, based on the SRIM predicted He profile. Bubble morphology appeared similar in both samples, consisting primarily of isolated bubbles that were largely spherical in shape.

4. Discussion

In this study, the He concentration (~6 at.%) required for observable bubble nucleation in pre-damaged (amorphous) Gd$_2$Ti$_2$O$_7$ is about a factor of 2 larger than the critical He concentration of 3 at.% estimated for observable bubble formation in amorphous borosilicate glass [16]. While bubbles 1–2 nm in diameter have been observed at concentrations as low as 0.12 at.% in borosilicate glass [17], bubbles are not observed in pre-damaged Gd$_2$Ti$_2$O$_7$ implanted with 2×10^{16} He/cm^2 (peak He concentration of 1 at.%), even after subsequent post-implantation irradiation at 300, 500 and 700 K. Bubbles are barely visible in the sample pre-damaged and implanted with 2×10^{17} He/cm^2. Since bubbles are not observed in the sample pre-damaged, implanted with 2×10^{16} He/cm^2, and post-damaged at both room and high temperature, the

additional irradiation damage does not appear to enhance He mobility or bubble nucleation in the pre-damaged $Gd_2Ti_2O_7$ containing up to 1 at.% He. Thermally induced He mobility in amorphous $Gd_2Ti_2O_7$ seems to remain low at 700 K, which agrees with the He desorption work performed by Wiss et al. on partially amorphous and fully amorphous $Gd_2Ti_2O_7$, where He release did not occur until a temperature of 900 K was reached [23]. The first desorption peak for the crystalline structures $Gd_2Zr_2O_7$ and $Nd_2Zr_2O_7$ occurred at 700 K, lower than the amorphous $Gd_2Ti_2O_7$ structure, which suggests a higher He mobility in crystalline pyrochlore than in amorphous pyrochlore. In this work, bubbles are larger and of higher density in pristine implanted $Gd_2Ti_2O_7$ than in amorphous implanted $Gd_2Ti_2O_7$, suggesting a higher He mobility in the pristine lattice. In the early stages (prior to amorphization) of He implantation into pristine $Gd_2Ti_2O_7$, the He may be more mobile than in amorphous $Gd_2Ti_2O_7$, leading to the formation of larger bubbles in the pristine implanted sample. Bubbles appeared circular in both samples implanted with 2×10^{17} He/cm^2, a morphology common to amorphous materials implanted with He.

5. Conclusion

This study highlights the capacity of amorphous $Gd_2Ti_2O_7$, one of the most widely considered materials for advanced nuclear waste immobilization, to accommodate large concentrations of He. Bubbles are not observable at He concentrations below ~6 at.%, which is a concentration level not expected in $Gd_2Ti_2O_7$ nuclear waste-forms until timescales exceeding 1 million years. Post-implantation irradiation damage does not affect bubble nucleation for the sample implanted with 2×10^{16} He/cm^2, even when irradiated at temperatures up to 700 K to enhance the kinetics of bubble formation. After implantation with up to 12 at.% He, individual bubbles are present within the $Gd_2Ti_2O_7$ matrix, but without fracturing the material. Additionally, this study examined the effects of an initially amorphous (pre-damaged) matrix, compared to a crystalline (pyrochlore) matrix on bubble nucleation and growth. Bubbles are larger and appear in higher densities when implanted in a crystalline $Gd_2Ti_2O_7$ matrix than in the amorphous matrix, even though a crystalline to amorphous phase transformation occurred during the He implantation of the sample that was not pre-damaged. Future work will aim to understand the mechanisms driving bubble nucleation in the crystalline matrix prior to amorphization, as well as in the amorphous matrix.

Appendix A. Supplementary data

Supplementary data related to this article can be found at http://dx.doi.org/10.1016/j.jnucmat.2016.07.043.

References

[1] R.C. Ewing, W.J. Weber, J. Lian, Nuclear waste disposal—pyrochlore ($A_2B_2O_7$): nuclear waste form for the immobilization of plutonium and "minor" actinides, J. Appl. Phys. 95 (2004) 5949–5971.
[2] I. Muller, W.J. Weber, Plutonium in crystalline ceramics in glasses, MRS Bull. 26 (2001) 698–706.
[3] W.J. Weber, R.C. Ewing, Chapter 10: Ceramic waste forms for uranium and transuranium elements, in: G.E. Burns PCS (Ed.), Uranium Cradle to Grave, Mineralogical Association of Canada Short Course, vol. 43, 2013, pp. 317–336. Winnipeg MB.
[4] W.J. Weber, R.C. Ewing, C.R.A. Catlow, T.D. De La Rubia, L.W. Hobbs, C. Kinoshita, H. Matzke, A.T. Motta, M. Nastasi, E.K.H. Salje, Radiation effects in crystalline ceramics for the immobilization of high-level nuclear waste and plutonium, J. Mater. Res. 13 (1998) 1434–1484.
[5] B.C. Chakoumakos, Systematics of the pyrochlore structure type, ideal $A_2B_2X_6Y$, J. Solid State Chem. 53 (1984) 120–129.
[6] M.A. Subramanian, G. Aravamudan, G.V.S. Rao, Oxide pyrochlores—a review, Prog. Solid State Chem. 15 (1983) 55–143.
[7] L. Minervini, R.W. Grimes, K.E. Sickafus, Disorder in pyrochlore oxides, J. Am. Ceram. Soc. 83 (2000) 1873–1878.
[8] K.E. Sickafus, L. Minervini, R.W. Grimes, J.A. Valdez, M. Ishimaru, F. Li, K.J. McClellan, T. Hartmann, Radiation tolerance of complex oxides, Science 289 (2000) 748–751.
[9] J. Lian, J. Chen, L.M. Wang, R.C. Ewing, J.M. Farmer, L.A. Boatner, K.B. Helean, Radiation-induced amorphization of rare-earth titanate pyrochlores, Phys. Rev. B 68 (2003) 134107.
[10] S.X. Wang, L.M. Wang, R.C. Ewing, G.S. Was, G.R. Lumpkin, Ion irradiation-induced phase transformation of pyrochlore and zirconolite, Nucl. Instrum. Methods Phys. Res. B 148 (1999) 704–709.
[11] B.D. Begg, N.J. Hess, D.E. McCready, S. Thevuthasan, W.J. Weber, Heavy-ion irradiation effects in $Gd_2(Ti_{2-x}Zr_x)O_7$ pyrochlores, J. Nucl. Mater. 289 (2001) 188–193.
[12] W.J. Weber, J.W. Wald, H. Matzke, Self-radiation Damage in Actinide Host Phases of Nuclear Waste Forms. vol. 44: Cambridge Univ Press, p.679.
[13] B.D.H. Begg, N J, W.J. Weber, R. Devanathan, J.P. Icenhower, S. Thevuthasan, B.P. McGrail, Heavy-ion irradiation effects on structures and acid dissolution of pyrochlores, J. Nucl. Mater. 288 (2001) 208–216.
[14] T. Wiss, O. Dieste-Blanco, A. Tacu, A. Janssen, Z. Talip, J.-Y. Colle, P. Martin, R. Konings, TEM study of alpha-damaged plutonium and americium dioxides, J. Mater. Res. 30 (2015) 1544–1554.
[15] T. Yang, C.A. Taylor, C. Wang, Y. Zhang, W.J. Weber, J. Xiao, J. Xue, S. Yan, Y. Wang, Effects of He irradiation on yttria-stabilized zirconia ceramics, J. Am. Ceram. Soc. 98 (2015) 1314–1322.
[16] G. Gutierrez, S. Peuget, J.A. Hinks, G. Greaves, S.E. Donnelly, E. Oliviero, C. Jegou, Helium bubble formation in nuclear glass by in-situ TEM ion implantation, J. Nucl. Mater. 452 (2014) 565–568.
[17] R. Bes, T. Sauvage, S. Peuget, J. Haussy, F. Chamssedine, E. Oliviero, T. Fares, L. Vincent, Helium mobility in SON68 borosilicate nuclear glass: a nuclear reaction analysis approach, J. Nucl. Mater. 443 (2013) 544–554.
[18] Y. Zhang, M.L. Crespillo, H. Xue, K. Jin, C.H. Chen, C.L. Fontana, J.T. Graham, W.J. Weber, New ion beam materials laboratory for materials modification and irradiation effects research, Nucl. Instrum. Methods Phys. Res. Sect. B Beam Interact. Mater. Atoms 338 (2014) 19–30.
[19] J.F. Ziegler, J.P. Biersack, U. Littmark, The Stopping Range of Ions in Solids, Pergamon Press, New York, 1985.
[20] Y. Zhang, I.T. Bae, K. Sun, C. Wang, M. Ishimaru, Z. Zhu, W. Jiang, W.J. Weber, Damage profile and ion distribution of slow heavy ions in compounds, J. Appl. Phys. 105 (2009) 104901.
[21] Y. Zhang, K. Jin, Z. Zhu, D.A. Grove, H. Xue, J. Xue, W.J. Weber, Electronic stopping powers for heavy ions in SiC and SiO_2, J. Appl. Phys. 115 (2014) 044903.
[22] W.S. Rasband; ImageJ; U.S. National Institutes of Health; Bethesda; Maryland, USA;http://imagej.nih.gov/ij/.
[23] T.A.G. Wiss, J.P. Hiernaut, P.M.G. Damen, S. Lutique, R. Fromknecht, W.J. Weber, Helium behaviour in waste conditioning matrices during thermal annealing, J. Nucl. Mater. 352 (2006) 202–208.